Article:
Calmé, B., Metcalf, A., Brockdorff, M. et al. (5 more authors) (2025) Hybrid Tendon-Actuated and Soft Magnetic Robotic Platform for Pancreatic Applications. IEEE Robotics and Automation Letters. ISSN 2377-3766

https://doi.org/10.1109/lra.2024.3524889

Hybrid Tendon-Actuated and Soft Magnetic Robotic Platform for Pancreatic Applications

Benjamin Calmé[1], Adam Metcalf[1], *Member*, IEEE, Michael Brockdorff[1], Haneul Jang[2], Yoonsue Choi[2], Peter Lloyd[1], Seok Chang Ryu[2], *Member*, IEEE and Pietro Valdastri[1], *Fellow*, IEEE

***Abstract*—Magnetic Soft Continuum Robots (MSCR) are used in a wide variety of surgical interventions, including neurological, pancreatic, and cardiovascular procedures. To function effectively, these MSCRs require complex programmable magnetisation. However, they often suffer from limited manoeuvrability and imprecise positioning of the devices that carry them. Tendon-Driven Continuum Robots (TDCR) have the potential to address these issues. These navigation systems not only enable higher accuracy and precision but also offer the potential for remote control, thereby reducing clinicians' exposure to ionising radiation. Currently, MSCRs are deployed from manual flexible endoscopes without motion compensation, leading to uncertainty and trial-and-error insertion. In this study, the deployment of high aspect ratio MSCRs (60 mm long by 1.3 mm diameter) from a tendon-driven robot (25 cm long with a 2.8 mm diameter) is performed. By precisely positioning the deployment point, this paper evaluates the benefits of different magnetisation profiles. The comparison is carried out for a specific clinical scenario, assessing procedure time, the distance between the external permanent magnet (used for steering) and the MSCR, and the interaction force with the tissue. Clinical relevance is demonstrated through pancreatic and bile duct cannulation in a silicon phantom.**

***Index Terms*—Magnetic Continuum Manipulators; Hybrid Actuation; Soft Robots; Medical Robotics.**

I. Introduction

SOFT robotics enables the design of compliant devices that ensure safe navigation without the risk of damage to the patient, holding great promise for medical applications [1]–[3]. MSCRs, due to their off-board actuation, have tremendous potential for miniaturisation, offering active steering and navigation in a remotely controllable manner by leveraging magnetic control along their entire length. The magnetic field has unique advantages for safely navigating robots inside the human body, such as high transparency to biological tissue and excellent controllability for field generation [4]. The wide range of catheter designs illustrated in the literature demonstrates the significant interest in this approach [5], [6].

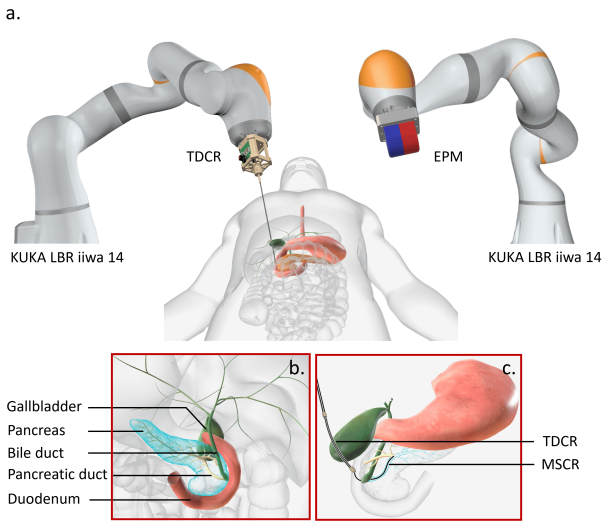

Fig. 1. Overview of the robotic platform, which includes two robotic arms: one controlling the proposed hybrid architecture (i.e., TDCR and MSCR) and the other managing the position of an external permanent magnet (a). Identification of the key anatomical elements (b). Illustration of the TDCR insertion and MSCR navigation (c).

Among these is a category of customisable MSCRs, allowing surgeons to tailor their design and specifications to meet the requirements of each individual procedure. These MSCRs, in which magnetised or magnetisable microparticles are uniformly dispersed in soft polymeric matrices, feature a predefined magnetic signature associated to the intended path [7]–[9]. However, while navigation demonstrations have been carried out for surgical applications—whether targeting peripheral nodules in the lungs [9], navigating narrow channels in the pancreas and gallbladder [10], or accessing deep areas of the brain [11]—it is crucial that the deployment boundary conditions are respected for the seamless execution of such procedures. One persistent challenge involves spatial errors of the endoscope tip, which can vary by up to 15 mm between the expected and measured values within a robotised platform [12]. This discrepancy results in imprecise positioning and motion of the MSCR base [10]. These errors can significantly influence the required actuating fields, leading to deviations from the intended trajectory [9]. This paper explores a hybrid architecture to overcome these limitations.

Manuscript received: 22 August 2024; Accepted 5 December 2024 .

This letter was recommended for publication by Editor J. Burgner-Kahrs upon evaluation of the reviewers' comments.

[1]Benjamin Calmé, Adam Metcalf, Michael Brockdorff, Peter Lloyd and Pietro Valdastri are with STORM Lab, Institute of Autonomous Systems and Sensing (IRASS), School of Electronic and Electrical Engineering, University of Leeds, UK b.p.calme@leeds.ac.uk

[2]Haneul Jang, Yoonsue Choi and Seok Chang Ryu are with Division of Mechanical and Biomedical Engineering, Ewha Womans University, Seoul, SK

This work was supported in one hand by the Engineering and Physical Sciences Research Council (EPSRC) under Grants EP/V047914/1 and EP/V009818/1, the European Research Council (ERC) through the European Union's Horizon 2020 Research and Innovation Programme under Grant 818045, the National Institute for Health and Care Research (NIHR) Leeds Biomedical Research Centre (BRC) (NIHR203331), and in an other hand by the National Research Foundation of Korea (NRF) Grant funded by the Korean Government (MSIT) under Grant 2021R1A2C2011854, RS-2023-00266145 and, in part by the Brain Korea 21 Four Program (Corresponding author: Benjamin Calmé.)

As demonstrated with other continuum robots, magnetic actuation can be combined with alternative driving mechanisms, such as TDCR, enabling the hybrid architecture to utilise the mobility characteristics of each individual method, thereby enhancing overall performance [13]–[16]. However, to the best of the authors' knowledge, this paper is the first to explore a hybrid design that amalgamates the benefits of hybrid actuation and hybrid stiffness. While other studies do involve hybrid actuation, none employ the soft-rigid hybridisation as described in this paper. The two closest works are reported in [16] and [14], which use tendon and magnetic actuation; however, neither incorporates stiffness hybridisation within their architecture. In particular, the robot described in [16] does not include a soft component, and although [14] introduced the use of a soft skin embedded with magnetic particles, the overall stiffness remains predominantly determined by the TDCR skeleton.

In clinical practice, cannulation of the bile and pancreatic ducts, shown in Fig.1.b, is performed using a duodenoscope. This approach involves selective cannulation of the bile and/or main pancreatic duct through the major duodenal papilla, an anatomical entry point. However, due to the mismatch in catheter diameter, this often necessitates a sphincterotomy of the papilla, which can lead to significant complications and long-term side effects for the patient [17]. The proposed robotic platform, illustrated in Fig.1.a, aims to achieve minimally invasive cannulation through a laparoscopic approach. Although the laparoscopic procedure remains invasive, the authors note that the side effects associated with laparoscopic insertion of the TDCR and the use of a soft catheter for cannulation, as depicted in Fig. 1.c, are considerably lower than those arising from a sphincterotomy [18].

Although TDCRs and MSCRs are independently well-studied types of robots, this letter proposes a combined approach to enhance overall performance. The novelty lies in their ability to work synergistically: the TDCR provides precise positioning and motion compensation, while the MSCR, when magnetically steered from a known position, safely navigates within a delicate tissue model. Importantly, they do not interfere with each other; the low stiffness of the MSCR preserves the TDCR's positioning performance, while the paramagnetic material of the TDCR ensures that it remains unaffected by the magnetic field guiding the MSCR.

This letter highlights (1) the use of TDCR for positioning and motion compensation to facilitate controlled MSCR deployment, (2) an exhaustive evaluation of various magnetisation profiles, and (3) the first evaluation of these capabilities using a single External Permanent Magnet (EPM).

II. SYSTEM OVERVIEW

A. The Tendon-Driven Continuum Robot

The TDCR consists of an etched Nitinol tube with notches that form two articulated sections operated by tendons. Two tendons are used and routed along the robot to allow for bending in one degree of freedom (planar bending). Since tendons cannot be pushed, using a single tendon allows for control of bending in only one direction. To achieve control in both directions of in-plane bending, a pair of antagonistic tendons, located on opposite sides of the compliant joints, is required. Both cables are anchored at the motor shaft, which can rotate in either direction, facilitating bending both ways while preventing any counteraction between the cables and backbone compression. Spatial bending is then achieved using the same principle as in the second section. Consequently, the robot includes a total of four tendons, comprising two antagonistic pairs.

These sections of the robot are designed with compliant joints arranged in series, such as thin, flexible segments between rigid sections, which can be fabricated monolithically. Due to their monolithic structure and intrinsic elasticity, compliant joints can bend continuously and are thus also referred to as continuum joints. The rectangular cuts that form these joints are produced using conventional subtractive manufacturing techniques, specifically femtosecond laser cutting. The first section (shorter and proximal) can achieve a total deflection of 30° in the XY plane, while the second allows for a total deflection of 60° in the XZ plane, as detailed in Fig. 2. This robotic component is actuated by stepper motors fixed to the base of the robot. The tube has an outer diameter of 2.8 mm and an inner channel diameter of 1.45 mm.

B. The Magnetically Soft Continuum Robot

The MSCR consists of a composite material made from silicone and hard-magnetic microparticles, e.g. neodymium-iron-boron NdFeB. These magneto-responsive materials can undergo various deformations driven by external magnetic forces and torques through the use of magnetic fields and gradients. To actuate the MSCRs, it is necessary to magnetically saturate the NdFeB particles. During this saturation phase, a specific magnetic signature can be embedded, which is predefined and conditions the overall behaviour of the MSCR in the presence of a magnetic field.

The MSCR is actuated in this work using a single EPM, differing from previous studies [9], [11] which use two independent permanent magnets. It is important to note that, unlike using two EPMs, a single EPM cannot produce both attraction and repulsion simultaneously (in two discrete locations), and the strength of the magnetic field and gradients cannot be independently controlled. However, using only one EPM makes the entire platform significantly less cumbersome, which could facilitate an easier transition to clinical applications. Implementing the proposed hybrid architecture within the previously described platform [9], [11] would require three manipulators: two to shape the MSCR and one to position the TDCR.

To align with the anatomical constraints of the pancreatobiliary tree, the MSCR features a high aspect ratio, measuring 60 mm in length with a 1.3 mm outer diameter. This soft robotic component also includes a 0.4 mm diameter channel along its centre. The purpose of this channel is to demonstrate the potential for the catheter to remain in place at the end of the cannulation procedure.

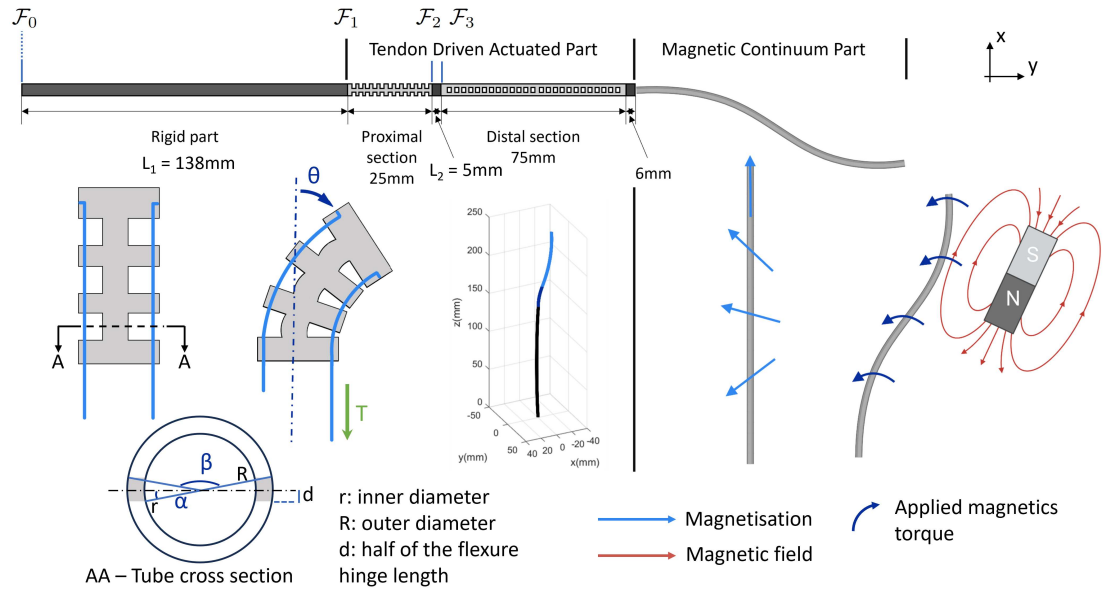

Fig. 2. Conceptual illustration of the hybrid robot. On the left: the cable-driven component, where tensioning a cable causes the tube to bend at the flexures. Each section bends in an orthogonal plane. On the right: the magnetically actuated section, where a soft segment containing particles magnetised according to a predefined profile can be controlled by applying a magnetic field. The identified geometric parameters and frames $\mathcal{F}_i|i = [0; 3]$ are utilised in the modelling Section III.

III. Modeling

A. TDCR model

In this work, each compliant section is assumed to have a piecewise-constant curvature, which facilitates straightforward robot-independent kinematic transformations [19].The transformation ${}^0\mathbf{T}_4$ describing the position and orientation of the tip relative to the base coordinate $\mathcal{F}_0$ can be formulated as follows:

$$ {}^0\mathbf{T}_4 = {}^0\mathbf{T}_1.{}^1\mathbf{T}_2.{}^2\mathbf{T}_3.{}^3\mathbf{T}_4 \tag{1}$$

The dimensions associated with the kinematics of the robot are defined in Fig. 2. ${}^0\mathbf{T}_1$ and ${}^2\mathbf{T}_3$ involve a simple translation from $\mathcal{F}_0$ to $\mathcal{F}_1$ and $\mathcal{F}_2$ to $\mathcal{F}_3$, along the axis by the length of the rigid part, respectively L_1 and L_2, as illustrated in Fig. 2.

$$ {}^0\mathbf{T}_1 = \begin{bmatrix} 1 & 0 & 0 & 0 \\ 0 & 1 & 0 & -L_1 \\ 0 & 0 & 1 & 0 \\ 0 & 0 & 0 & 1 \end{bmatrix}, \quad {}^2\mathbf{T}_3 = \begin{bmatrix} 1 & 0 & 0 & 0 \\ 0 & 1 & 0 & -L_2 \\ 0 & 0 & 1 & 0 \\ 0 & 0 & 0 & 1 \end{bmatrix} \tag{2}$$

The curvature of a joint is defined as $r_i|i = 1, 2$. The initial, i.e. undeformed, length of each section is denoted by $l_{s_i|i=1,2}$. When the proximal section is actuated by the tendon, it deforms by an angle θ_1. The homogeneous transformation matrix for this joint is given by:

$$ {}^1\mathbf{T}_2 = \begin{bmatrix} C_{\theta_1} & -S_{\theta_1} & 0 & (1 - C_{\theta_1})/r_1 \\ S_{\theta_1} & C_{\theta_1} & 0 & -S_{\theta_1}/r_1 \\ 0 & 0 & 1 & 0 \\ 0 & 0 & 0 & 1 \end{bmatrix}, \quad \text{with } r_1 = \frac{\theta_1}{l_{s1}} \tag{3}$$

Where C and S represent cosine and sine, respectively. In the same way, ${}^3\mathbf{T}_4$ describes the curvature of the distal section, r_2 following a deformation by an angle θ_2.

$$ {}^3\mathbf{T}_4 = \begin{bmatrix} 1 & 0 & 0 & 0 \\ 0 & C_{\theta_2} & -S_{\theta_2} & -S_{\theta 2}/r_2 \\ 0 & S_{\theta_2} & C_{\theta_2} & (C_{\theta_2} - 1)/r_2 \\ 0 & 0 & 0 & 1 \end{bmatrix}, \quad \text{with } r_2 = \frac{\theta_2}{l_{s2}} \tag{4}$$

It is noted that the total joint curvature r_i can be approximated by the superposition of the bending angles of all individual tubes within the notch. This approximation indicates a linear relationship between the curvature r_i, the bending stiffness κ and the tendon-pulling reaction moment M

$$ M = \kappa r \tag{5}$$

from which it is possible to derive the relationship between tendon tension T, the bending stiffness and the curvature

$$ T = \frac{r\kappa}{d} \tag{6}$$

where d is the distance from the tendon to the centre. Here, the tendon is approximated to run parallel to the centroidal axis. This equation indicates that the beam curvature is directly controlled by the cable tension, with the moment arm to bending stiffness ratio acting as a gain factor. The stiffness of a flexure can be described as a function of Young's modulus E, the second moment of area I_x and the flexure length w, as

$$ \kappa = EI_x, \quad \text{with } I_x = \iint y^2 dA \tag{7}$$

Considering a rectangular cut in the tube, the cross sectional area A of the flexure is derived as follows:

$$ A = \pi R^2 - 2\left(\frac{R^2}{2}(\beta - \sin(\beta)) + d\sqrt{R^2 - d^2} + \alpha r^2\right) \tag{8}$$

where R and r are the outer and inner radii of the tube, respectively, and d, β and α are geometric parameters defined in Fig. 2.

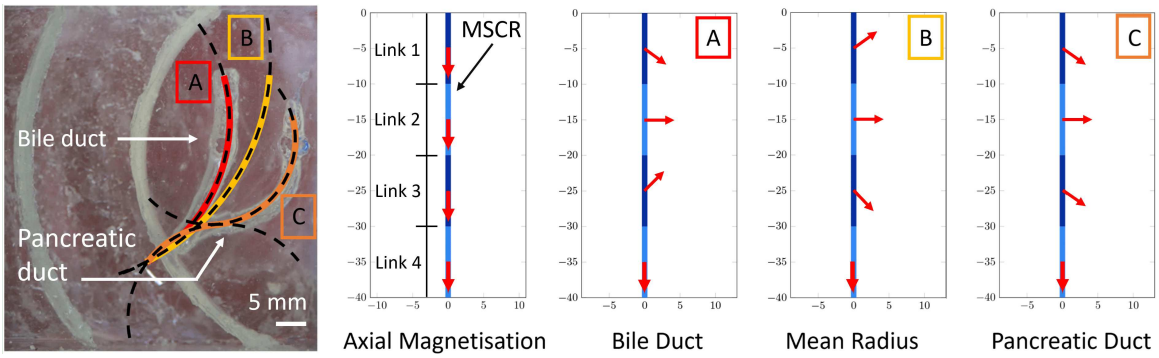

Fig. 3. Different magnetisation profiles for navigating the anatomical phantom. On the left, the dashed lines indicate the radii used for optimisation, while the solid line shows the intended shape of the tentacle based on the magnetisation profiles depicted on the right. The MSCR is shown in blue, with red arrows indicating the magnetisation directions for each link.

B. MSCR model

The clinical scenario under study involves deploying the MSCR into both the pancreatic and bile ducts. With an expected stable deployment point established, various magnetisation profiles are compared to a simple axial magnetisation. Specifically, a dedicated magnetisation profile for each duct, tailored to the patient and procedure, is compared with a more general magnetic profile that should be deployable into either duct by adjustment of only the applied magnetic field.

1) Magnetic Profile

The MSCR is modelled as a serial chain of rigid links connected by planar rotational joints, as described in [20], simplifying the approach presented in [10]. The desired shape of the MSCR can be represented by a vector of joint angles $\mathbf{q}$, with the size of $\mathbf{q}$ depending on the level of discretisation and the variable length of the MSCR, which is a function of time. The elastic joint torque is expressed as follows:

$$\boldsymbol{\tau}_q = \frac{\boldsymbol{K}\mathbf{q}}{l} \tag{9}$$

where l is the virtual link length and $\boldsymbol{K}$ is the elastic stiffness such as

$$\boldsymbol{K} = \text{diag}(E_x I_x \;\; E_y I_y \;\; E_z I_z) \tag{10}$$

The magnetic torque $\boldsymbol{\tau}$ exerted on a magnetic dipole of moment $\mathbf{m} \in \mathbb{R}^3$ when subjected to an external actuating field $\mathbf{B} \in \mathbb{R}^3$ can be derived as

$$\boldsymbol{\tau}_{mag(t)} = \mathbf{m} \times \mathbf{B}(t) \tag{11}$$

The torque balance was achieved according to [20] by enforcing the constraint that the distal magnetisation must be axial, providing a stable and reliable reference direction for the magnetic field vector. Additionally, also for stability reasons, the magnetisation process was configured such that all segment magnetisations must remain within 60° of their neighbouring segment magnetisations. The solution was computed using the Genetic Algorithm (GA, Global Optimisation Toolbox, MATLAB version R2023b) to generate four-link discretised magnetisation profiles and four time-stepping actuating fields, as detailed and evaluated in [9], [20].

The driving variable in this context is the bending radius r, as detailed in Tab. I and illustrated in Fig. 3. This radius is defined as the radius of the circle formed by the array of equal desired joint angles. Therefore, taking q_{des} as a scalar from the joint angle array and l as the virtual link length, r is derived as:

TABLE I
VALUES OF THE CURVATURE RADII USED IN THE MODEL TO DERIVE EACH MAGNETISATION PROFILE

r_{bile}[A]	r_{mean}[B]	$r_{pancreas_1}$[C]	$r_{pancreas_2}$[C]
58 mm	67 mm	18 mm	33 mm

$$r = \frac{l}{2\sin\left(q_{des}\right)} \tag{12}$$

Consequently, if the position along the robot's length from the tip is defined as S, the magnetisation m at any point along the robot is given by:

$$\mathbf{m} = |\mathbf{m}|\text{rot}_z\left(\frac{S}{\pi r}180°\right)\hat{\mathbf{x}} \tag{13}$$

The output magnetisation profiles from the optimisation are therefore a sinusoidal pattern running along the robot's long axis, the x-axis.

2) EPM poses

Compared to [20], where the field is applied using a 3-D electromagnetic coil, in this case an EPM connected to a serial robotic arm is used. Two assumptions are made, the first being that both $\mathbf{B}$ and $\mathbf{m}$ are constrained to a single plane, and secondly, that the EPM is positioned to create a magnetic field considered homogeneous (or, in practice, the effects of any actuating gradients are negligible). According to the dipole model, the magnetic field from the EPM is related to its pose as follows:

$$\mathbf{B} = \frac{\mu_0|\boldsymbol{m}|}{4\pi|\mathbf{p}|^3}\left(3\hat{\mathbf{p}}\hat{\mathbf{p}}^{\mathrm{T}} - \boldsymbol{I}_3\right)\hat{\boldsymbol{m}}, \tag{14}$$

where $\mathbf{p} \in \mathbb{R}^3$ represents the position of the EPM, μ_0 is the magnetic permeability of free space ($4\pi \times 10^{-7}$ N.A^{-2}), and $|.|$ denotes the Euclidean norm, with $\hat{\cdot} = \frac{\cdot}{|\cdot|}$.

Adapting [9], the pose of the EPM, for the desired field, derived from the optimisation, is then given by:

$$|\mathbf{p}| = \left(\frac{2\pi|\mathbf{B}|}{\mu_0|\boldsymbol{m}|}\right)^{\frac{1}{3}} \tag{15}$$

$$\hat{\boldsymbol{m}} = \frac{\left(3\hat{\mathbf{p}}\hat{\mathbf{p}}^{\mathrm{T}} - \mathbf{I}_3\right)^{-1}}{|3\hat{\mathbf{p}}\hat{\mathbf{p}}^{\mathrm{T}} - \mathbf{I}_3|}\hat{\mathbf{B}} \tag{16}$$

Similar to [21], using the calibration data from the optical tracker, $\mathbf{p}$ and $\hat{\boldsymbol{m}}$ are transformed into an end-effector pose for the robot, which is then commanded via the inverse kinematics of the robot arm.

IV. IMPLEMENTATION

This section details the fabrication of the TDCR and MSCR, which are combined with the robotic platform and validated in Section V.

A. TDCR Fabrication

The tubular delivery platform consists of two integral parts interconnected by a holder system: a tendon-driven instrument made from metal tubes and an actuation module for pulling and releasing the tendons. The holder system not only aligns these components but also ensures the secure placement of tendons within designated channels.

The instrument itself is a composite structure, featuring a distal section made from a laser-machined NiTi tube (JMM19841, Johnson Matthey, United Kingdom, OD/ID: 1.95/1.65 mm) and a proximal section constructed from Stainless Steel 304 tubing (OD/ID: 2.8/2.5 mm). The differing material rigidities result in negligible deformation of the proximal part while allowing for controlled bending of the distal segment when Kevlar tendons are pulled. Tendon alignment is achieved through a multi-lumen outer tube (Pebax 5533 SA 01 MED, ARKEMA, France) and 3D-printed fixtures bonded to the tubes with epoxy. The NiTi tube is precision-machined using a femtosecond laser (Starcut Tube SL, Coherent, USA), forming 55 H-shaped units to ensure uniform compliance. Each unit is 1 mm long and 0.5 mm wide, with bending rigidity varying with the unit angle (θ). This setup is calibrated to achieve its maximum bend angle with a 15 N tendon force.

The actuation module integrates a motor control and power board (U2D2 PHB, ROBOTIS, Republic of Korea) and a compact DC motor (AX-12A, ROBOTIS, Republic of Korea) within a 3D-printed frame (Form 3, Clear resin, Formlabs, USA). A 3D-printed circular disk attached to the motor facilitates the pulling and releasing of tendons in both directions.

B. MSCR Fabrication

The MSCRs were fabricated by mixing Dragon Skin 30 (Smooth-On Inc, USA) with NdFeB microparticles in a 1:1 mass ratio. This composite was mixed and degassed in a high vacuum mixer (ARV-310, THINKYMIXER, Japan) at 1400 rpm, 20.0 kPa for 90 seconds. The mixture was then injected into a 3D-printed mold (Clear resin, Form3+, Formlab) and cured in an oven for 30 min at 45°C before removal.
Although resin printers can produce precise and detailed moulds for casting thin MSCRs, the photoinitiator in the resin can induce silicone cure-inhibition [22]. To prevent this issue, the two parts were washed with isopropyl alcohol (IPA) and coated with a mould release agent (Smooth-On) before moulding. After unmoulding, the tentacle was cured a second time in an oven at 45°C for a further 30 minutes.

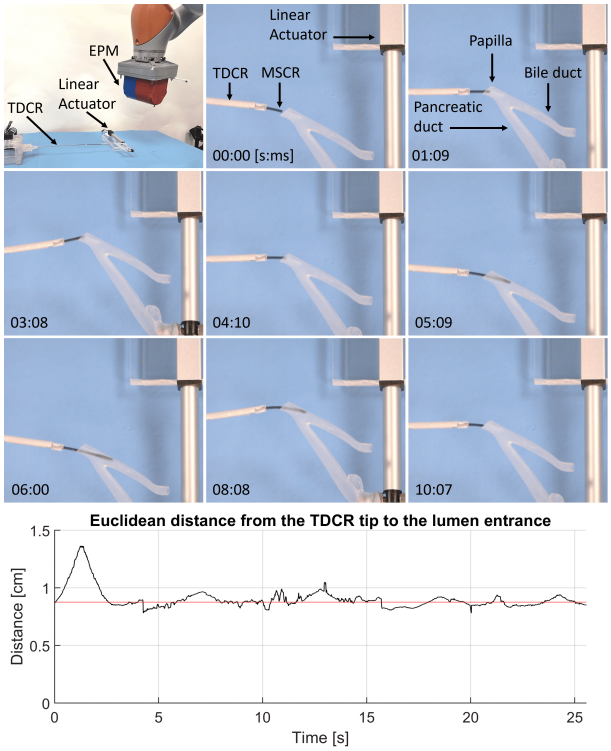

Fig. 4. Demonstration of 25.5 mm amplitude and 0.2 Hz motion compensation using the TDCR to ensure accurate deployment of the MSCR relative to the lumen entrance. Lumen motion was achieved through a linear actuator, while compensation via the TDCR maintained a consistent distance of 8 mm, enabling precise steering of the MSCR.

To assign the optimised magnetic moment to each segment, 3D-printed trays (Clear resin, Form3+, Formlabs) were fabricated, each with a specified magnetisation direction. The MSCR was then exposed to a saturating uniform magnetic field of 4.644 T (ASC IM-10-30, ASC Scientific, USA).

V. DEMONSTRATION OF CLINICAL APPLICATION

The experiments aim to demonstrate the benefits of combining the TDCR and the MSCR. To achieve this, the authors first illustrate the advantages of using the TDCR for precise positioning through motion compensation, which ensures proper insertion of the MSCR and reduces friction. This characterisation involves different metrics such as insertion time, EPM distance, and contact force evaluation.

A. Positioning and motion compensation

As previously introduced, the MSCR requires proper positioning to be deployed, indeed the optimisation for the magnetisation is calculated assuming an initial deployment position with respect to the lumen entrance. The inherent dexterity of the TDCR allows the deployment point to be positioned properly or correct for a positional offset resulting from the insertion within the tissue. As illustrated in Fig. 4, TDCR dexterity allows to keep the MSCR deployment point in front of the papilla. A 3D printed phantom of the pancreatobiliary tree was horizontally fixed to a linear actuator (L12-30-50-6-R, Actuonix, Canada), achieving a 25.5 mm

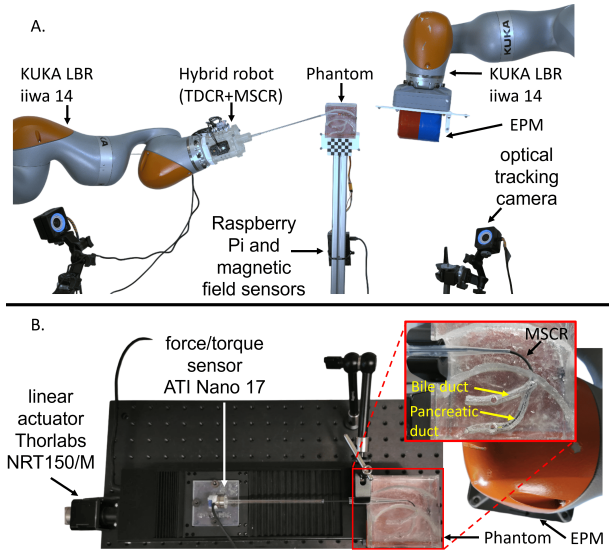

Fig. 5. Experimental setup for the robotic platform (A) within a mock clinical scenario, and (B) for evaluation of contact forces.

displacement at a frequency of 0.2 Hz, equivalent to the breathing cycle. Then using the model described in Sec. III-A, the TDCR was controlled to match the breathing motion, ensuring the tip remained aligned with the papilla. Once the synchronisation is achieved, a KUKA LBR iiwa14 robot (KUKA, Germany) handling an EPM with a cylindrical shape, measuring 101.6 mm in diameter and length, and possessing an axial magnetisation of 970.1 Am² (Grade N52), was used to steer the MSCR inside the lumen.

B. Evaluation of Magnetic Profiles

Considering a proper deployment point, the proposed platform is used to characterise the effectiveness of different magnetic profiles to navigate into the bile and pancreatic ducts of a 1:1 scale ultrasoft phantom representing the duodenum and biliary-pancreatic tree. The phantom was cast in silicone (Ecoflex™ Gel, Smooth-On), following the method described in [21]. This material was chosen for its Shore hardness of 00-35, closely replicating the softness of the pancreas and bile environment [23]. Two sets of experiments were conducted to assess the system's performance and compare the various magnetisation profiles.

For the second set of experiments, a dual-arm platform was used. The hybrid robot was mounted on the end-effector of the first manipulator, while the second manipulator was responsible for handling an EPM. Ground truth data was collected using a 4-camera optical tracking system (OptiTrack Prime 13, NaturalPoint, Inc., USA). Optical markers were affixed to the end-effectors of both robots and to the base of the phantom's acrylic box. The relative pose of each robotic arm and the phantom with respect to the world coordinate system was determined before each experiment (see Fig. 5). While the EPM was in motion, its pose was tracked by reading the joint angles of the robotic arms and computing the forward kinematics, ensuring accurate motion tracking even if the markers were obstructed from view during movement. A hall effect sensor (MLX90395, Melexis, Belgium. Sensing range

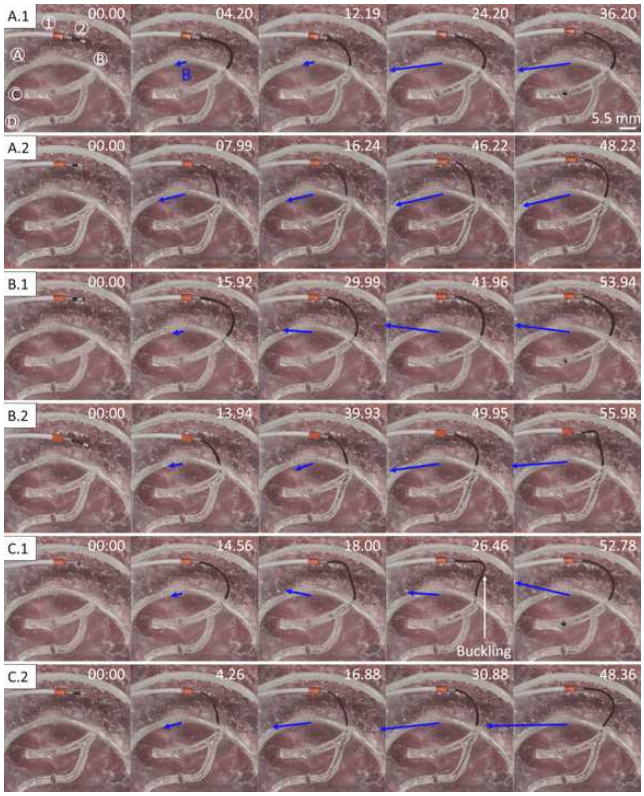

Fig. 6. Timed snapshots of different insertions with axial magnetisation (A), mean magnetisation (B), and specific magnetisation (C) in the bile duct (1) and the pancreatic duct (2). The first snapshot highlights the TDCR (1) and the MSCR (2), as well as the anatomical structures: duodenum (A), major papilla (B), bile duct (C), and pancreatic duct (D). The blue arrow indicates the magnitude and direction of the applied magnetic field. [Time unit: Second]

± 50 mT; Sensitivity 2.5 μT/LSB16; Footprint $3 \times 3 \times 0.9$ mm) connected to a Raspberry Pi was positioned at the rear of the phantom to ensure that the magnetic field was applied correctly. All components, including the Raspberry Pi, robotic arms, and optical tracking system, were interconnected via ROS.

The MSCR was attached to a thin Nitinol wire with a 200μm diameter, allowing it to be deployed through the TDCR working channel. Markers were engraved on the wire to correspond with the length of each segment, facilitating insertion control and robot arm adjustments based on the EPM pose derivation using the model described in Sec. III-B2. A chequerboard was positioned at the base of the phantom to calibrate the Basler camera and aid in post-experiment analysis.

Insertion was performed manually to simulate catheterisation during the first set of experiments, assessing the system under realistic conditions. Each duct was subsequently lubricated with PolyDiMethylSiloxane (PDMS) silicone oil of viscosity 20 cSt (Sigma-Aldrich Inc.) to lubricate and mimic the aqueous nature of internal anatomy. Three magnetisation profiles were evaluated, and insertion processes were recorded. Fig. 6 illustrates the progression of insertion through the lumen at various time intervals for the three MSCR types. Videos of the insertion processes for the three scenarios are shown in the Supplementary Video [24]. Tab. II summarise the results from the insertion repetitions, three per scenario, including recorded

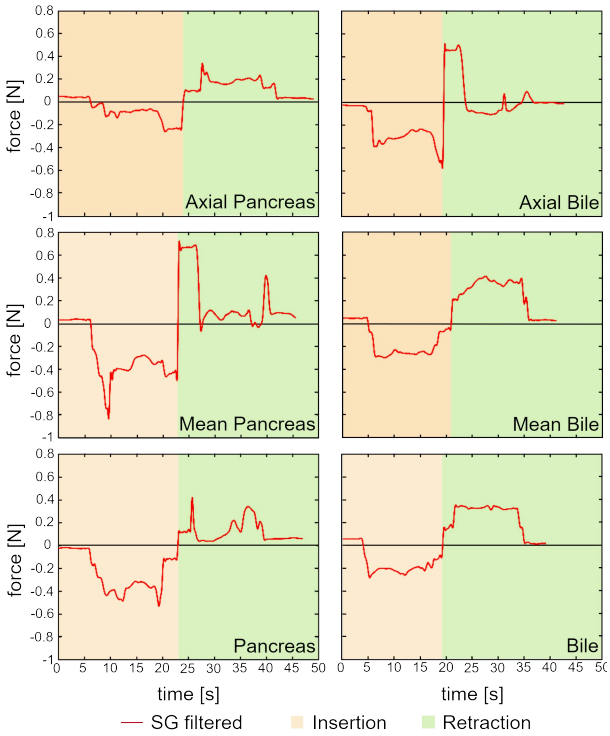

Fig. 7. Absolute maximum force values measured during the insertion and retraction of the MSCR after applying an adaptive Savitzky-Golay smoothing filter.

procedure time, maximum depth reached, EPM distance from the phantom, and the risk of buckling during insertion. Buckling episodes were categorised as follows: '+' indicates 1 to 3 episodes, and '++' indicates 3 to 7 (maximum) episodes.

For the third set of experiments, the MSCR was inserted into the channel similarly to the earlier tests but was now controlled using a linear actuator (Thorlabs NRT150/M) along the x-axis of the phantom. To isolate the insertion force and eliminate interactions with the side walls of the TDCR, the MSCRs were guided and pushed directly into the ducts of the soft phantoms. The MSCR was connected to the linear actuator via a force/torque sensor (Nano 17, ATI Corporation), enabling the measurement of the insertion force in all directions. Compared to the first experiment, motorised insertion enables controlled insertion and allows for the acquisition of contact force and torque values. This approach eliminates, for example, operator tremor, ensuring that only measurements specific to the contact are performed. As shown in Fig. 7, only the maximum values for Fx are reported, as forces in other directions were significantly lower and thus disregarded. The raw data signals were filtered using a Savitzky-Golay filter for easier interpretation. Insertion and retraction force tests were conducted by advancing the MSCR into the phantom at a speed of 3 mm/s while recording the time-stamped force. Experiments for each tentacle design and lumen combination were repeated three times.

VI. RESULTS AND DISCUSSION

In these experiments, the deployment of MSCRs from the TDCR and their navigation through the pancreatobiliary tree were evaluated, stabilising the position of the deployment point in case of motion of the target anatomy and comparing the performance of different magnetic profiles. The MSCRs were optimised for patient-specific ducts, deployed from the TDCR, and remotely actuated via an external permanent magnet. Successful cannulations were demonstrated in an ultrasoft, realistic phantom. The presented platform, consisting of a 2.8 mm OD TDCR and a 1.3 mm OD, 60 mm long MSCR, enables deep insertion into the different ducts.

The first experiment highlights the interest of using the TDCR to carry the MSCR, while its dexterity ensures deployment as stated during the optimisation. This is highlighted by an error of 1.9 mm$\pm$0.3 mm during motion compensation. The mean position error value of the TDCR tip after deployment in the second experiments is 1.2 mm$\pm$0.1 mm, with a maximum value of up to 2.3 mm. The highest values were reached during or following buckling of the MSCR. Even if not perfect, compared to standard conditions, the position of the TDCR tip is considered stable, as hypothesised from the start. It should be noted that the positioning error is also linked to the robotic manipulator; however, as its resolution is 0.1 mm, it was considered negligible.

Axially magnetised MSCR can be seen to conform to the complex trajectories of the ducts, leading to physical interactions with the surrounding environment. Despite these interactions, the MSCR were always able to reach the target. It is worth noting that torsion along the axis can help rotate the MSCR during insertion. While the contact force remained comparable to that with optimised complex magnetisation during insertion, lower contact forces were observed during bile duct retraction, though higher forces were recorded in the pancreatic duct. This discrepancy is attributed to the normal contact force related to the path's convolution. The bile duct, with its C-shaped configuration, is easier to navigate compared to the S-shaped pancreatic duct, where axial magnetisation acts like tendon pulling, causing a higher interaction force attributed to tissue deformation. Procedures with axially magnetised MSCRs were quicker, with insertion times 30% and 45% faster for the bile duct compared to mean and specific magnetisation profiles, respectively. The difference for the pancreatic duct was less pronounced, at 8% and 6%, respectively. These results should be considered alongside insertion depth, where axially magnetised MSCRs reached a final depth at least 19% deeper than with mean magnetisation and at least 8% deeper than with specific magnetisation.

During the experiments, it was observed that the optimally magnetised MSCRs also experienced some torsion around their main axis during the final state, occasionally causing undesirable behaviour due to instability. This made control strategies more challenging. Despite requiring more time, their performance was comparable to that of axially magnetised MSCRs in terms of insertion depth, and they achieved retraction from complex paths with the lowest contact force.

The mean magnetisation profile, intended to fit both ducts, was less reliable. It created more contact, complicating insertion into more complex paths and leading to increased buckling. It failed to achieve the insertion depth of the other two magnetisation profiles. This finding suggests that any bespoke magnetisation needs to be highly trajectory specific and not generic for "similar" navigations.

TABLE II
VALUE OF THE CURVATURE RADII USED IN THE MODEL FOR OBTAINING EACH OF THE MAGNETISATION PROFILES

	Insertion Time [s]	Retraction Time [s]	Overall procedure Time [s]	Insertion Depth [mm]	EPM distances* [cm]	Buckling
Ax. mag. B	36.2	32.2	117.9	63	20.3 / 10.94	
Ax. mag. P	48.2	52.0	166.8	65	29.5 / 13.82	
Mean mag. B	53.9	55.9	170.0	51	24.19 / 9.62 / 13.26	
Mean mag. P	75.2	30.3	181.9	47	24.19 / 13.33 / 7.77	+
Spe. mag. B	52.8	66.0	216.1	57	24.19 / 17.19 / 9.48 / 13.13	++
Spe. mag. P	68.2	42.0	172.9	60	24.19 / 13.4 / 7.07 / 6.14	++

Ax: Axial; mag: magnetisation; Spe: Specific *Distance between the different poses of the EPM and the papilla + Buckling episodes

It was noted that using a single EPM for complex magnetisation profiles may not always be optimal. Experiments showed that the robot is at risk of entering a zone close to the patient's body (less than 10 cm). Axial magnetisation allows the EPMs to be positioned further away from the patient while still ensuring a functional magnetic field.

While these results favour using axial magnetisation with a single EPM, results may differ with two EPMs, as suggested by [9]. One result aligning with this hypothesis is the lower contact force observed during retraction from the pancreatic duct with an MSCR featuring a dedicated magnetic profile. However, optimisation using braiding [10] is necessary, as axial torque and instability are issues pertaining to complex magnetisation profiles. Considering this statement, two scenarios seem preferable for future applications: either using a single EPM with axial magnetisation for paths of low and moderate complexity or a dual EPM platform with a complex magnetisation profile and embedded mechanical reinforcing for highly convoluted paths.

This work relies on preoperative planning, visual sensing and open-loop control. In real clinical scenarios, feasible navigation cannot be guaranteed without real-time tracking of the MSCR and anatomy in a low or zero visibility environment. Future work will incorporate intra-operative imaging (e.g., CT or ultrasound) and shape sensing of the MSCR (e.g., fiber Bragg gratings) to ensure navigation via closed-loop control.

ACKNOWLEDGMENT

Any opinions, findings and conclusions, or recommendations expressed in this article are those of the authors and do no necessarily reflect the views of the NRF, MSIT, EPSRC, ERC, NIHR, BRC, or the Department of Health and Social Care.

REFERENCES

[1] M. Cianchetti, C. Laschi, A. Menciassi, and P. Dario, "Biomedical applications of soft robotics," *Nature Reviews Materials*, vol. 3, 2018.

[2] P. E. Dupont, B. J. Nelson, M. Goldfarb, B. Hannaford, A. Menciassi, M. K. O'Malley, N. Simaan, P. Valdastri, and G.-Z. Yang, "A decade retrospective of medical robotics research from 2010 to 2020," *Science Robotics*, vol. 6, no. 60, Nov. 2021.

[3] P. E. Dupont, N. Simaan, H. Choset, and C. Rucker, "Continuum Robots for Medical Interventions," *Proceedings of the IEEE*, Jul. 2022.

[4] Z. Yang, H. Yang, Y. Cao, Y. Cui, and L. Zhang, "Magnetically Actuated Continuum Medical Robots: A Review," *Advanced Intelligent Systems*, vol. 5, no. 6, 2023.

[5] Y. Kim, G. A. Parada, S. Liu, and X. Zhao, "Ferromagnetic soft continuum robots," *Science Robotics*, vol. 4, no. 33, Aug. 2019.

[6] R. Dreyfus, Q. Boehler, S. Lyttle, P. Gruber, J. Lussi, C. Chautems, S. Gervasoni, J. Berberat, D. Seibold, N. Ochsenbein-Kölble, M. Reinehr, M. Weisskopf, L. Remonda, and B. J. Nelson, "Dexterous helical magnetic robot for improved endovascular access," *Science Robotics*, vol. 9, no. 87, Feb. 2024.

[7] W. Hu, G. Z. Lum, M. Mastrangeli, and M. Sitti, "Small-scale soft-bodied robot with multimodal locomotion," *Nature*, vol. 554, no. 7690, pp. 81–85, Feb. 2018.

[8] T. Xu, J. Zhang, M. Salehizadeh, O. Onaizah, and E. Diller, "Millimeter-scale flexible robots with programmable three-dimensional magnetization and motions," *Science Robotics*, vol. 4, no. 29, Apr. 2019.

[9] G. Pittiglio, J. H. Chandler, T. da Veiga, Z. Koszowska, M. Brockdorff, P. Lloyd, K. L. Barry, R. A. Harris, J. McLaughlan, C. Pompili, and P. Valdastri, "Personalized magnetic tentacles for targeted photothermal cancer therapy in peripheral lungs," *Communications Engineering*, vol. 2, no. 1, pp. 1–13, Jul. 2023.

[10] P. Lloyd, O. Onaizah, G. Pittiglio, D. K. Vithanage, J. H. Chandler, and P. Valdastri, "Magnetic Soft Continuum Robots With Braided Reinforcement," *IEEE Robotics and Automation Letters*, Jul. 2022.

[11] Z. Koszowska, M. Brockdorff, T. da Veiga, G. Pittiglio, P. Lloyd, T. Khan-White, R. A. Harris, J. W. Moor, J. H. Chandler, and P. Valdastri, "Independently Actuated Soft Magnetic Manipulators for Bimanual Operations in Confined Anatomical Cavities," *Advanced Intelligent Systems*, vol. 6, no. 2, 2024.

[12] B. Bardou, P. Zanne, F. Nageotte, and M. de Mathelin, "Control of a multiple sections flexible endoscopic system," in *2010 IEEE/RSJ International Conference on Intelligent Robots and Systems*, Oct. 2010.

[13] S. Wu, Q. Ze, J. Dai, N. Udipi, G. H. Paulino, and R. Zhao, "Stretchable origami robotic arm with omnidirectional bending and twisting," *Proceedings of the National Academy of Sciences*, Sep. 2021.

[14] T. Zhang, L. Yang, X. Yang, R. Tan, H. Lu, and Y. Shen, "Millimeter-Scale Soft Continuum Robots for Large-Angle and High-Precision Manipulation by Hybrid Actuation," *Advanced Intelligent Systems*, 2021.

[15] Q. Peyron, Q. Boehler, P. Rougeot, P. Roux, B. J. Nelson, N. Andreff, K. Rabenorosoa, and P. Renaud, "Magnetic concentric tube robots: Introduction and analysis," *The International Journal of Robotics Research*, vol. 41, no. 4, pp. 418–440, Apr. 2022.

[16] G. Pittiglio, M. Mencattelli, A. Donder, Y. Chitalia, and P. E. Dupont, "Hybrid Tendon and Ball Chain Continuum Robots for Enhanced Dexterity in Medical Interventions," in *2023 IEEE/RSJ International Conference on Intelligent Robots and Systems (IROS)*, Oct. 2023.

[17] P. B. Cotton, D. A. Garrow, J. Gallagher, and J. Romagnuolo, "Risk factors for complications after ERCP: a multivariate analysis of 11,497 procedures over 12 years," *Gastrointestinal Endoscopy*, Jul. 2009.

[18] S. R. Singh SS, "Minimally invasive gastrointestinal surgery: A review," *Cureus*, 2023.

[19] D. B. Camarillo, C. F. Milne, C. R. Carlson, M. R. Zinn, and J. K. Salisbury, "Mechanics Modeling of Tendon-Driven Continuum Manipulators," *IEEE Transactions on Robotics*, pp. 1262–1273, 2008.

[20] P. Lloyd, T. L. Thomas, V. K. Venkiteswaran, G. Pittiglio, J. H. Chandler, P. Valdastri, and S. Misra, "A Magnetically-Actuated Coiling Soft Robot With Variable Stiffness," *IEEE Robotics and Automation Letters*, vol. 8, no. 6, pp. 3262–3269, Jun. 2023.

[21] M. Brockdorff, T. da Veiga, J. Davy, P. Lloyd, J. H. Chandler, G. Pittiglio, R. K. Mathew, and P. Valdastri, "Hybrid trajectory planning of two permanent magnets for medical robotic applications," *The International Journal of Robotics Research*, Jul. 2024.

[22] B. Venzac, S. Deng, Z. Mahmoud, A. Lenferink, A. Costa, F. Bray, C. Otto, C. Rolando, and S. Le Gac, "PDMS Curing Inhibition on 3D-Printed Molds: Why? Also, How to Avoid It?" *Analytical Chemistry*, vol. 93, no. 19, pp. 7180–7187, May 2021.

[23] A. Tejo-Otero, F. Fenollosa-Artés, I. Achaerandio, S. Rey-Vinolas, I. Buj-Corral, M. M.T, and E. Engel, "Soft-tissue-mimicking using hydrogels for the development of phantoms," *Gels*, vol. 8, 2022.

[24] B. Calmé, "Supplementary Video." [Online]. Available: https://youtu.be/eT5bjOxIdJk